npj | vaccines

Article

Published in partnership with the Sealy Institute for Vaccine Sciences

https://doi.org/10.1038/s41541-024-01060-2

A KIF20A-based thermosensitive hydrogel vaccine effectively potentiates immune checkpoint blockade therapy for hepatocellular carcinoma

Xingyang Zhao[1], Feichao Xuan[1], Zirong Li[1], Xiangyi Yin[1], Xiaojun Zeng[1], Jiali Chen[1] & Chihua Fang[1,2,3,4] ✉

Hepatocellular carcinoma (HCC) is a highly prevalent malignancy with limited treatment efficacy despite advances in immune checkpoint blockade (ICB) therapy. The inherently weak immune responses in HCC necessitate novel strategies to improve anti-tumor immunity and synergize with ICB therapy. Kinesin family member 20A (KIF20A) is a tumor-associated antigen (TAA) overexpressed in HCC, and it could be a promising target for vaccine development. This study confirmed KIF20A as a promising immunogenic antigen through transcriptomic mRNA sequencing analysis in the context of HCC. Therefore, we developed a thermosensitive hydrogel vaccine formulation (K/R^{Lip}@Gel) to optimize antigen delivery while enabling sustained in vivo release. The vaccine efficiently elicited robust immune responses by activating DCs and T cells. Moreover, K/R^{Lip}@Gel improved the therapeutic efficacy of PD-L1 blockade in subcutaneous and orthotopic cell-derived xenograft (CDX) models, along with immune-humanized patient-derived xenograft (PDX) HCC models, which was evidenced by improved maturation of DCs and elevated infiltration and activation of CD8$^+$ T cells. These findings highlight the potential of KIF20A-based vaccines to synergistically improve ICB therapy outcomes in HCC, providing a promising approach for enhancing anti-tumor immunity and improving clinical outcomes.

Hepatocellular carcinoma (HCC) is one of the most prevalent and deadly malignancy worldwide[1]. As recommended by serval clinical guidelines, immune checkpoint blockade (ICB) therapy has become a widely adopted approach for HCC treatment in combination with anti-angiogenesis therapy, a strategy that activates anti-tumor immunity to a certain extent[2–5]. Although the regimen realizes superior outcomes compared to targeted therapy and chemotherapy, its median overall survival (mOS) and objective response rate (ORR) are still limited[6–8]. Consequently, only a restricted patient group benefits from the treatment, signifying the need for novel complementary strategies to stimulate the immune responses more effectively[9,10].

Cancer vaccines directly prime the host immune system against cancer and potentially improve the efficacy of ICB therapy[11,12]. And the antigens used for vaccine development are classified as tumor-associated antigens (TAAs) or neoantigens, with TAAs representing overexpressed self-proteins within tumors and neoantigens arising from tumor-specific mutations[13]. Both classes have been explored for HCC treatment. However, recent studies indicate that neoantigens could rarely be detected in the human leukocyte antigen (HLA) ligandomes of HCC, while unmutated TAAs are frequently presented, indicating that vaccines targeting TAAs could provide a more promising strategy for HCC treatment[14]. Although several TAAs have been the target of vaccines investigated in clinical trials for HCC, the outcomes have been unsatisfactory. These challenges could be primarily attributed to the low antigen immunogenicity, inefficient antigen delivery to antigen-presenting cells (APCs), premature antigen degradation, or the lack of coordinated adjuvants. Therefore, there is a need to consider antigen immunogenicity and optimize vaccine formulations, including adjuvants and delivery systems, to enhance therapeutic outcomes[15–17].

[1]First Department of Hepatobiliary Surgery, General Surgery Center, Zhujiang Hospital, Southern Medical University, Guangzhou, China. [2]Institute of Digital Intelligent Minimally Invasive Surgery, Zhujiang Hospital, Southern Medical University, Guangzhou, China. [3]Guangdong Provincial Clinical and Engineering Center of Digital Medicine, Guangzhou, China. [4]South China Institute of National Engineering Research Center of Innovation and Application of Minimally Invasive Instruments, Guangzhou, China. ✉e-mail: fangchihua@smu.edu.cn

Identifying an optimal antigen to target a particular tumor type has long been a priority for developing cancer vaccine[18]. Kinesin family member 20A (KIF20A) plays significant roles in mitosis and is upregulated in different malignancies[19–21]. Recent studies have revealed that the KIF20A knockdown potentiates the therapeutic efficacy of ICB therapy of HCC[22]. Moreover, KIF20A has been investigated as a TAA across various cancers. However, its suitability for HCC has not yet been explored[23,24]. Due to its overexpression in HCC and its correlation with poor prognosis, KIF20A could be a promising target for inducing an effective immune response in HCC[25,26]. When incorporated into well-designed vaccine formulations, KIF20A could improve treatment efficacy of ICB, providing a more precise and effective treatment strategy for HCC patients.

In this study, we identified that KIF20A as a potential antigen that was suitable for HCC vaccination using transcriptomic mRNA sequencing analysis. Then, a KIF20A-based vaccine formulation was designed, in which KIF20A protein and adjuvant R848 were encapsulated in cationic liposomes to realize stable and efficient delivery to antigen-presenting dendritic cells (DCs). A biocompatible PLGA-PEG-PLGA thermosensitive hydrogel was incorporated to realize sustained antigen and adjuvant release. The immune activation effect of the vaccine was confirmed with primary DCs and T cells, and its efficacy in improving the therapeutic effect of PD-L1 blockade therapy, a commonly used ICB strategy for HCC treatment, was assessed in cell-derived HCC xenograft (CDX) and immune-humanized patient-derived HCC xenograft (PDX) models. This is the first study to demonstrate the suitability of KIF20A as an antigen for HCC treatment while eliciting effective immune responses, including DCs and $CD8^+$ cells. Therefore, the study preliminarily provides a new strategy for developing an HCC vaccine and improving the ICB therapy outcomes in HCC patients.

Results

KIF20A is a potential antigen for eliciting anti-HCC immune responses

Differentially expressed genes (DEGs) were analyzed between the control and KIF20A groups. Compared to the control group, 2550 genes were upregulated while 531 were downregulated (Supplementary Fig. 1a). Gene expression patterns were consistent within each group but differed between the control and KIF20A groups (Supplementary Fig. 1b). Gene Ontology (GO) enrichment analysis indicated significant upregulation of genes associated with biological process (BP) linked with immune activation, such as leukocyte migration, positive regulation of the immune system process, phagocytosis, and leukocyte chemotaxis (Fig. 1a). Additionally, cellular component (CC) genes, including those involved in endoplasmic reticulum lumen, endoplasmic reticulum lumen, secretory granule lumen, and endocytic vesicle, indicating improved immune cell function, were upregulated[27–29]. Furthermore, genes linked with immune-related molecular function (MF), such as immune receptor activity, cytokine binding, and pattern recognition receptor activity, exhibited significant upregulation. Kyoto Encyclopedia of Genes and Genomes (KEGG) enrichment analysis depicted the upregulation of immune-related pathways, including cytokine-cytokine receptor interaction, leukocyte transendothelial migration, T cell receptor signaling pathway, and efferocytosis (Fig. 1b)[30–32]. Furthermore, gene set enrichment analysis (GSEA) validated that gene upregulation involved in immune responses correlated with KIF20A protein treatment (Fig. 1c). Meanwhile, single-sample GSEA (ssGSEA) suggested a noticeable immune activation in the KIF20A group (Fig. 1d). The spleens and inguinal lymph nodes, both of which are important immune organs, were harvested for volume quantification using a vernier caliper, revealing significant volume growth in the KIF20A group compared to the control group (Supplementary Fig. 2, 3).

Design and characterization of KIF20A-based thermo-sensitive hydrogel vaccine

To evaluate the potential of KIF20A for HCC therapy, a KIF20A-based vaccine was developed using cationic liposome and hydrogel formulations for optimizing the antigen delivery efficacy. First, KIF20A protein and the adjuvant R848 were co-encapsulated in liposomes (indicated as K/R^{Lip}) to protect and co-deliver two agents, thereby efficiently facilitating APC activation[33–35]. Both encapsulation efficiency (EE) and encapsulation capacity (EC) were calculated to assess the drug loading properties of the liposomes. The EE of KIF20A protein and R848 were 86.75% and 68.92%, and the EC was 3.64% and 11.64%, respectively, depicting effective encapsulation of both agents. Transmission electron microscopy (TEM) highlighted the spherical morphology of the K/R^{Lip} and ICG-labeled liposomes (ICG-K/R^{Lip}), demonstrating nearly 104.20 nm in size (Fig. 2a and Supplementary Fig. 4a). Dynamic light scattering (DLS) analysis depicted the similar hydrated diameters of K/R^{Lip} (108.67 nm) and ICG-K/R^{Lip} (109.67 nm) (Fig. 2b). Moreover, K/R^{Lip} and ICG-K/R^{Lip} showed comparable diameter distributions, suggesting that the ICG loading did not change the liposome morphology significantly (Supplementary Fig. 4b). However, the Zeta potential of ICG-K/R^{Lip} was lower than K/R^{Lip}, possibly because of the negative charge of sulfonic acid group in ICG (Fig. 2c). The dispersion stability of K/R^{Lip} and ICG-K/R^{Lip} were confirmed over seven days, with hydrated diameter and Zeta potential remaining stable (Fig. 2d). Drug release studies at pH 7.4 and 5.6, simulating the extracellular matrix and lysosomal environments, revealed low release rates of R848 (10.27%) and KIF20A protein (8.30%) at pH 7.4, while the release rates increased to 60.87% and 41.80% at pH 5.6, respectively, indicating that the liposomes remained stable extracellularly but efficiently released their payloads in lysosomes (Fig. 2e,f). A previous study demonstrated that the pH-dependent release pattern of DOTAP liposomes although DOTAP is not inherently pH-sensitive[36], the mechanism underlying this pH-dependent release remains uncertain. To address this, we propose the following hypotheses: under acidic conditions, the decreased availability of anions enhances the overall positive charge of DOTAP, increasing electrostatic repulsion among DOTAP molecules. This destabilization of the liposomal membrane enables cargo release. Additionally, the reduced negative charge of KIF20A proteins weakens their electrostatic interactions with the cationic DOTAP lipids, promoting their release from the liposomes. Another study reported the remarkable cargo release rate from the DOTAP liposome in alkaline environment, indicating that the cargo release behavior could be affected by multiple factors[37].

PLGA-PEG-PLGA triblock copolymers were successfully synthesized and characterized by proton nuclear magnetic resonance (^{1}H-NMR) spectroscopy (Supplementary Fig. 5). Then, liposomes were added into the PLGA-PEG-PLGA solution to develop the thermosensitive hydrogel vaccine (K/R^{Lip}@Gel). The vaccine solution underwent gelation from a fluid state after incubating in a 37 °C-water bath for 5 min (Fig. 2g). Environmental scanning electronic microscopy (ESEM) images indicated the surface topography of K/R^{Lip}@Gel at 37°C (Fig. 2h) and highlighted the embedded liposomes in the hydrogel matrix (depicted by red arrows, Fig. 2i). Rheological analysis demonstrated that the gelation temperature was 36.17 °C, at which storage modulus (G') exceeded loss modulus (G"), validating the thermosensitive gelation property (Fig. 2j). Mechanical stability of the gel was demonstrated without significant changes in G' and G" for 6 min at 37 °C under constant shear stress of 1% amplitude with 1 rad/s (Fig. 2k). The results highlighted a thermosensitive property of the K/R^{Lip}@Gel allowing the subcutaneous vaccine injection and gelation at physiological temperature.

The absorbance and fluorescence spectra of ICG-K/R^{Lip}@Gel were determined, showing a 28-nm red shift in absorbance compared to free ICG, possessing similar fluorescence spectra (Fig. 2l, m). The subcutaneous retention rate of free ICG, nanoscale ICG-K/R^{Lip}, and gel-state ICG-K/R^{Lip}@Gel was evaluated using the second near-infrared (NIR-II) fluorescence imaging (Fig. 2n). Quantitative analysis depicted a prolonged release effect for ICG-K/R^{Lip}@Gel compared to ICG and ICG-K/R^{Lip}. This is evidenced by the significantly higher signal intensity at 96 h of ICG-K/R^{Lip}@Gel (Fig. 2o).

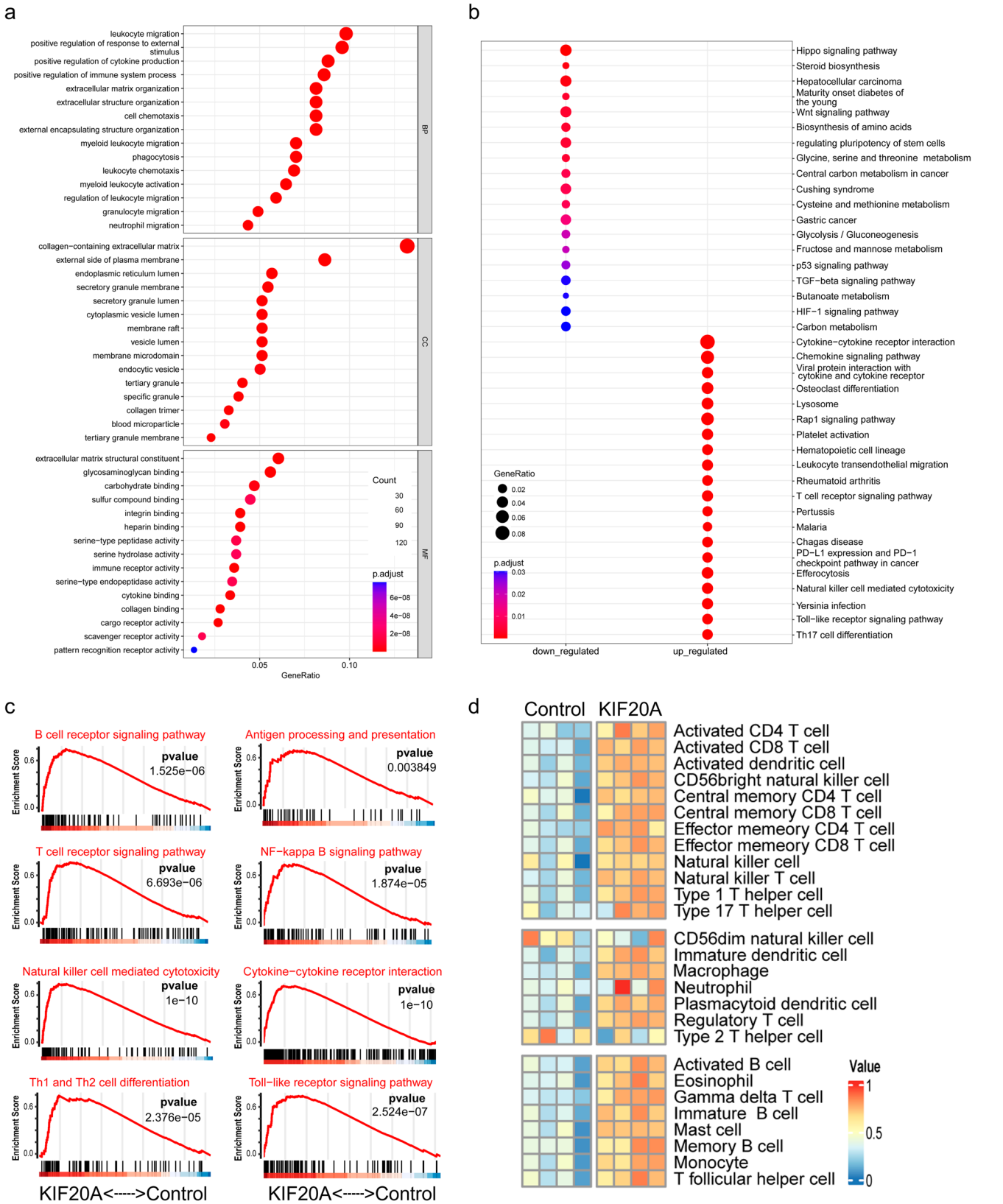

Fig. 1 | Transcriptomic mRNA sequencing analysis of mouse tumors in different groups. a GO enrichment analysis. **b** KEGG enrichment analysis. **c** GSEA. **d** ssGSEA.

K/R^{Lip}@Gel mediated co-delivery of KIF20A and R848 improved Dendritic and T cell responses

Mouse bone marrow-derived dendritic cells (BMDCs) and splenic T cells were used for in vitro experiments to assess the immune activation performance of the K/R^{Lip}@Gel vaccine. Before the experiments, the sterilized K/R^{Lip}@Gel was added into 6-well plates and solidified at 37 °C. BMDCs were divided into four groups, and the cell suspensions were added to the RPMI1640 culture medium and incubated using the solidified gel containing various payloads. After incubation for 24 h, the cells were harvested for flow cytometry. The percentage of CD80^{+}CD86^{+} within the CD11c^{+}

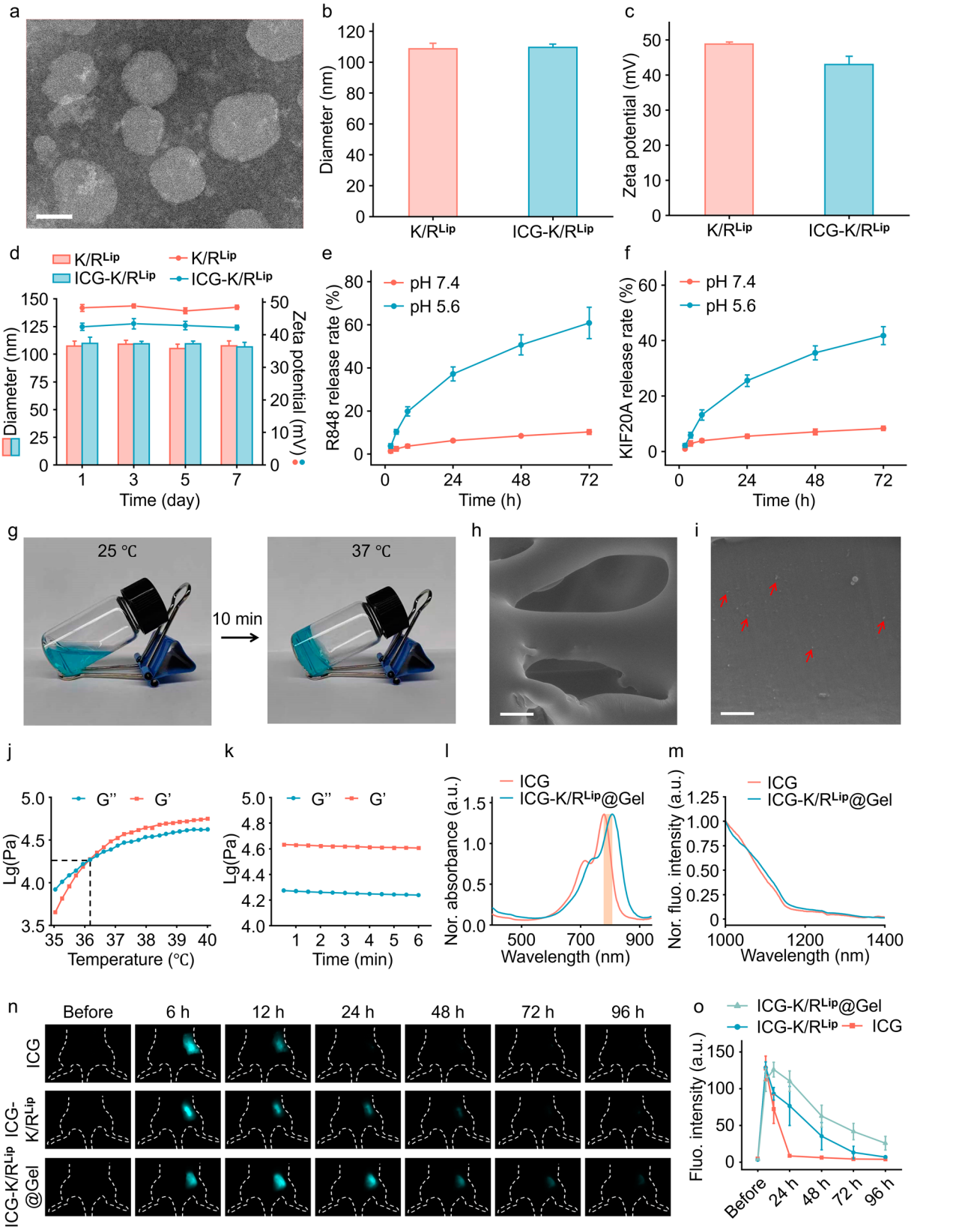

Fig. 2 | Characterization of the vaccine K/R^{Lip} and K/R^{Lip}@Gel. a TEM image of K/R^{Lip}. Scalebar: 100 nm. **b** Hydrated diameter of K/R^{Lip} and ICG-K/R^{Lip}. **c** Zeta potentials of K/R^{Lip} and ICG- K/R^{Lip}. **d** Hydrated diameter and Zeta potentials K/R^{Lip} on the 1, 3, 5 and 7 days. **e** R848 release rate of K/R^{Lip} at the pH of 7.4 and 5.6. **f** KIF20A release rate of K/R^{Lip} at the pH of 7.4 and 5.6. **g** Photographs of K/R^{Lip}@Gel at 25 °C and 37 °C. **h** ESEM image of K/R^{Lip}@Gel at 37 °C. **i** Liposomes (K/R^{Lip}) detected with ESEM (Red arrows). **j** Rheological analysis quantifying storage modulus (G') and loss modulus (G") of K/R^{Lip}@Gel at different temperatures. **k** Rheological analysis of gel stability for 6 min. **l** Absorbance spectra of ICG and ICG-K/R^{Lip}@Gel. **m** Fluorescence spectra of ICG and ICG- K/R^{Lip}@Gel. **n** NIR-II fluorescence images of mice injected with small molecule ICG, nanoscale ICG-K/R^{Lip} and hydrogel ICG-K/R^{Lip}@Gel. **o** Quantification of NIR-II fluorescence intensity at different time points after injections.

dendritic cells was quantified, indicating 70.37% of $CD80^+CD86^+$ dendritic cells in the K/R^{Lip}@Gel group, which was significantly higher than the other three groups (Fig. 3a, b). Additionally, the highest proportions of MHC-I^+ and MHC-II^+ cells were gated within the K/R^{Lip}@Gel group (Fig. 3c, e), accounting for 56.30% and 46.83%, respectively (Fig. 3d, f). The results from BMDC preliminarily demonstrated the potential of the K/R^{Lip}@Gel vaccine, highlighting the most efficient BMDC activation effect with the co-delivery of KIF20A and adjuvant R848.

Furthermore, we evaluated the ability of the vaccine-pulsed BMDCs to activate T cells. T cell proliferation was first assessed by co-incubating CFDA-SE-labeled splenocytes with vaccine-pulsed BMDCs for 3 days, followed by flow cytometry analysis of CFDA-SE intensity in $CD3^+$ T cells. Cells with reduced CFDA-SE intensity were characterized as proliferating T cells (Fig. 3g). The K/R^{Lip}@Gel group showed a significantly higher proportion of proliferating T cells than the other groups. Thus, K/R^{Lip}@Gel most effectively promoted T cell proliferation through BMDC activation (Fig. 3h). Additionally, the infiltration effect of the $CD8^+$ T cells across different groups into Hepa1-6 cell spheroids was visualized with confocal laser scanning microscopy (CLSM) (Fig. 3i). The infiltration rate, quantified as the ratio of T cell fluorescence ratio to DAPI fluorescence, was the highest in the K/RLip@Gel group, accounting for 19.13% (Fig. 3j). These results indicated the superior ability of BMDCs pulsed with K/R^{Lip}@Gel to activate T cells. Therefore, K/R^{Lip}@Gel exhibited great potential to elicit robust immune responses to within HCC cells.

Vaccination of K/R^{Lip}@Gel suppressed Hepa1-6 tumor growth

The biocompatibility of K/R^{Lip}@Gel was assessed before in vivo experiments. L929 skin fibroblasts incubated with K/R^{Lip}@Gel for 5 days indicated relatively high viability of 89.94%, showing minimal cytotoxicity (Supplementary Fig. 10). Additionally, the hemolysis assay depicted no significant difference in hemolysis rates between Gel, K/R^{Lip}@Gel, and negative control group (Supplementary Fig. 11). The results highlighted the excellent biocompatibility of K/R^{Lip}@Gel.

To evaluate the tumor-killing effect of the vaccine components, R^{Lip}@Gel, K^{Lip}@Gel, or K/R^{Lip}@Gel was subcutaneously injected to orthotopic Hepa1-6 tumor models at day 1 and 5. The tumor growth was monitored with bioluminescence imaging (Supplementary Fig. 12a). On day 13 post-treatment, both R^{Lip}@Gel and K^{Lip}@Gel demonstrated a significant tumor-killing effect compared to the control group, with K^{Lip}@Gel exhibiting a more pronounced therapeutic effect (Supplementary Fig. 12b). However, the K/R^{Lip}@Gel group revealed the most robust therapeutic outcomes, indicating the synergistic potential of combining KIF20A and R848 in the vaccine formulation.

Furthermore, healthy mice were subcutaneously vaccinated using K/R^{Lip}@Gel to determine the efficacy of activated immunity against HCC. After 3 days post-vaccination, Hepa1-6-luc cells were injected either orthotopically or subcutaneously and allowed to grow for 6 days. On day 9, the growth rates of orthotopic and subcutaneous tumors were monitored with bioluminescence imaging (Supplementary Fig. 13). The results depicted a significantly slower growth rate in the K/R^{Lip}@Gel compared to the Gel group for both tumor models. Therefore, the immune response elicited by K/R^{Lip}@Gel efficiently targeted HCC, thereby delaying tumor growth in mice.

K/R^{Lip}@Gel enhanced PD-L1 blockade therapy for CDX model

Orthotopic Hepa1-6-luc tumor-bearing mice were randomly divided into four groups and received varied treatments. The PD-L1 blockade (aPD-L1) group received intraperitoneal injections of PD-L1 antibody, and the K/R^{Lip}@Gel group received subcutaneous injections of K/R^{Lip}@Gel. In contrast, the aPD-L1 + K/R^{Lip}@Gel group received both treatments (Fig. 4a). Tumor growth was monitored with bioluminescence imaging at 3-day intervals over 13 days (Fig. 4b). By day 13, quantification of the bioluminescence signal intensity indicated a significant decrease in the aPD-L1 + K/R^{Lip}@Gel group compared to the other three groups, revealing the superior antitumor effect of the combination of K/R^{Lip}@Gel and PD-L1 antibody (Fig. 4c). No significant differences could be detected in body weight between the four groups, preliminarily highlighting the biosafety of the treatments (Fig. 4d). Moreover, inguinal lymph nodes, tumor tissues, spleens and blood samples were obtained for flow cytometry analysis at the end of the monitoring period. Quantification of $CD80^+CD86^+$ cells within $CD11c^+$ dendritic cells of inguinal lymph nodes suggested a significant elevation in the K/R^{Lip}@Gel and aPD-L1 + K/R^{Lip}@Gel groups compared to the control group (Fig. 4e, f), suggesting enhanced antigen presentation capability induced by vaccination. A similar maturation trend could be observed in splenic DCs. However, the overall proportion of $CD80^+CD86^+$ DCs in the spleen in each group was lower than the inguinal lymph nodes, possibly due to the preferential vaccine accumulation in the lymph nodes, which often serve as primary sites of immune activation after subcutaneous administration (Supplementary Fig. 16). In tumor tissue, an elevated population of $CD8a^+$ T cells was observed in the aPD-L1 + K/R^{Lip}@Gel group (Fig. 4g, h), with similar results detected across the spleens and blood samples (Supplementary Fig. 17, 18). Other than DCs and T cells, the function and polarization of tumor-associated macrophages were also assessed, indicating the significantly elevated proportion of anti-tumor $CD86^+$ macrophages (Supplementary Fig. 19). Thus, K/R^{Lip}@Gel effectively enhanced the outcomes of PD-L1 blockade therapy by stimulating the antitumor immune activity.

The therapeutic efficacy was further confirmed in subcutaneous HCC models, where the alterations in tumor size were more intuitively evident (Supplementary Fig. 20a, b). Tumor volume changes in different groups were recorded, showing the lowest relative tumor volume of aPD-L1 + K/R^{Lip}@Gel group on day 16 (Supplementary Fig. 20c). No significant difference could be detected in body weight among the groups during the monitoring period (Supplementary Fig. 20d). After the treatment monitoring period, the harvested tumors underwent histological analysis. Hematoxylin and eosin (H&E) staining depicted increased infiltrated cells and reduced tumor cell nuclei density (Supplementary Fig. 20e). In contrast, immunofluorescence showed an increased population of $CD8a^+$ cells in the aPD-L1 + K/R^{Lip}@Gel group (Supplementary Fig. 21). Moreover, F4/80 and CD11c were stained as the biomarkers for DCs and macrophages, respectively. The results indicated a slight increase in $F4/80^+$ macrophages in aPD-L1, K/R^{Lip}@Gel, and aPD-L1 + K/R^{Lip}@Gel groups compared to the control group. In contrast, evident increments in $CD11c^+$ DCs could be observed in the K/R^{Lip}@Gel and aPD-L1 + K/R^{Lip}@Gel groups, with the highest $CD11c^+$ proportion detected within the aPD-L1 + K/R^{Lip}@Gel group (Supplementary Fig. 22). H&E sections of lung, liver, spleen, kidney, and heart revealed no obvious pathological changes under optical microscopy (Supplementary Fig. 23). Additionally, the serum biochemical indexes indicating liver and kidney function, including ALT, AST, ALB, TBIL, CR and BUN, showed no apparent changes among the groups at the end of monitoring (Supplementary Fig. 24).

K/R^{Lip}@Gel improved PD-L1 blockade therapy for the PDX model

The immune-humanized PDX models were established by intravenously injecting human peripheral blood mononuclear cells (PBMCs) into mice (Supplementary Fig. 25a). Subsequently, the proportion of human $CD45^+$ ($hCD45^+$) cells in peripheral blood was quantified weekly with flow cytometry (Supplementary Fig. 25b). The successful model establishment was depicted by $hCD45^+$ cell levels exceeding 25%. Moreover, the H&E staining of different passages of tumor sections indicated the successful model establishment, and the immunohistochemistry result of P4 revealed the PD-L1 positive expression (Supplementary Fig. 25c).

The immune-humanized PDX mice were randomly divided into four groups and subjected to different treatment regimens. Subsequent tumor size measurements demonstrated a significant reduction in tumor volume in the aPD-L1 + K/R^{Lip}@Gel group, underscoring the improved therapeutic efficacy of aPD-L1 in combination with K/R^{Lip}@Gel (Fig. 5a, b). All the groups showed a consistent weight loss trend, potentially attributed to the induced graft-versus-host reaction (GVHR) (Fig. 5c).

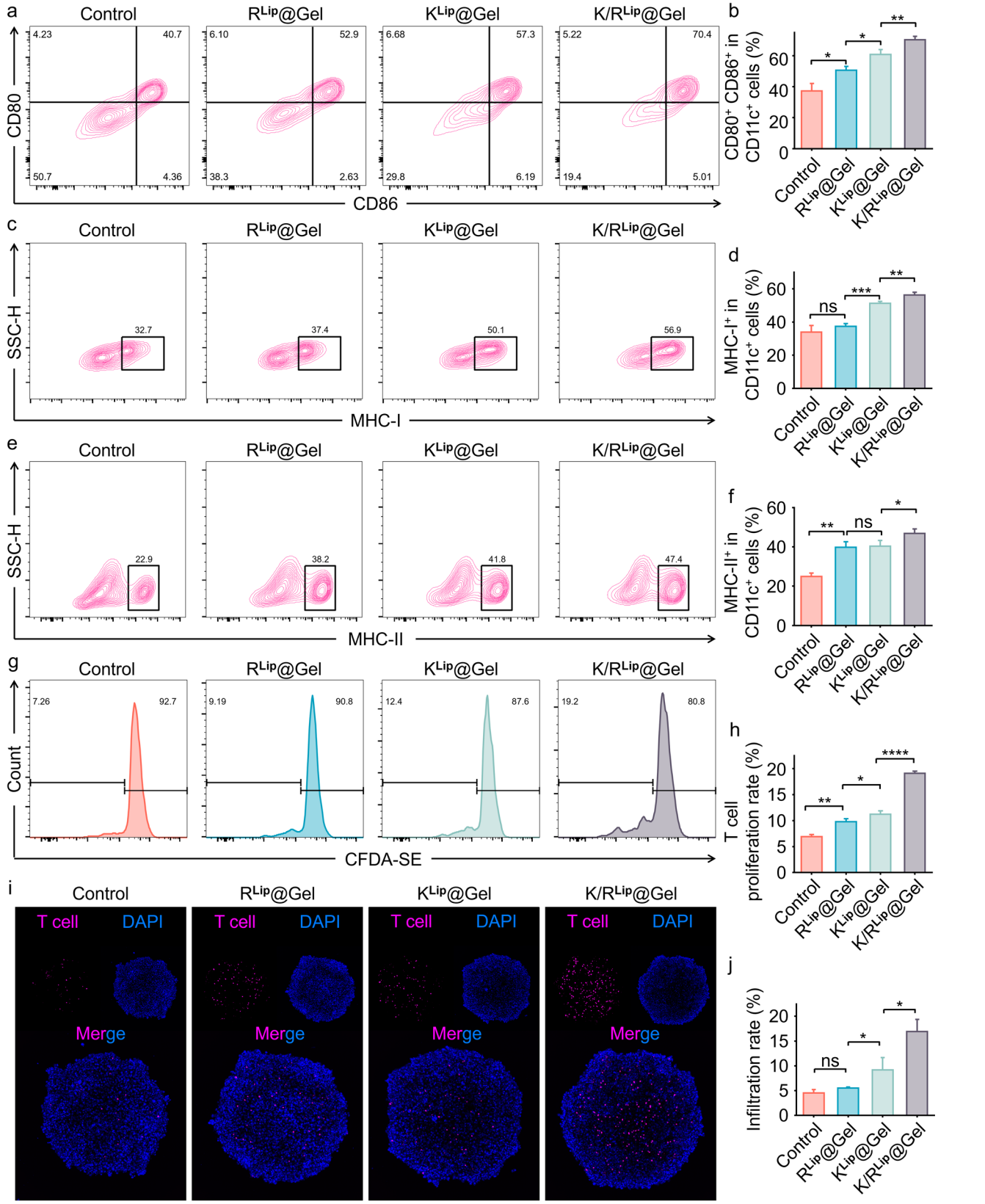

Fig. 3 | In vitro analysis of BMDC and T cell response to the hydrogel vaccine K/R^{Lip}@Gel. a CD80 and CD86 levels of BMDCs in flow cytometry (The gating strategy was shown in the Supplementary Fig. 6). **b** Quantification of the proportion of CD80$^+$CD86$^+$ BMDCs. **c** MHC-I level of BMDCs indicated by flow cytometry (The gating strategy was shown in the Supplementary Fig. 7). **d** Quantification of the proportion of MHC-I$^+$ BMDCs. **e** MHC-II level of BMDCs in flow cytometry (The gating strategy was shown in the Supplementary Fig. 8). **f** Quantification of MHC-II$^+$ BMDCs. **g** CFDA-SE level in CD3$^+$ T cells (The gating strategy was shown in the Supplementary Fig. 9). **h** Quantification of T cell proliferation rate. **i** CLSM images of infiltrated CD8a$^+$ T cells into Hepa1-6 cell spheroids. **j** Quantification of T cell infiltration.

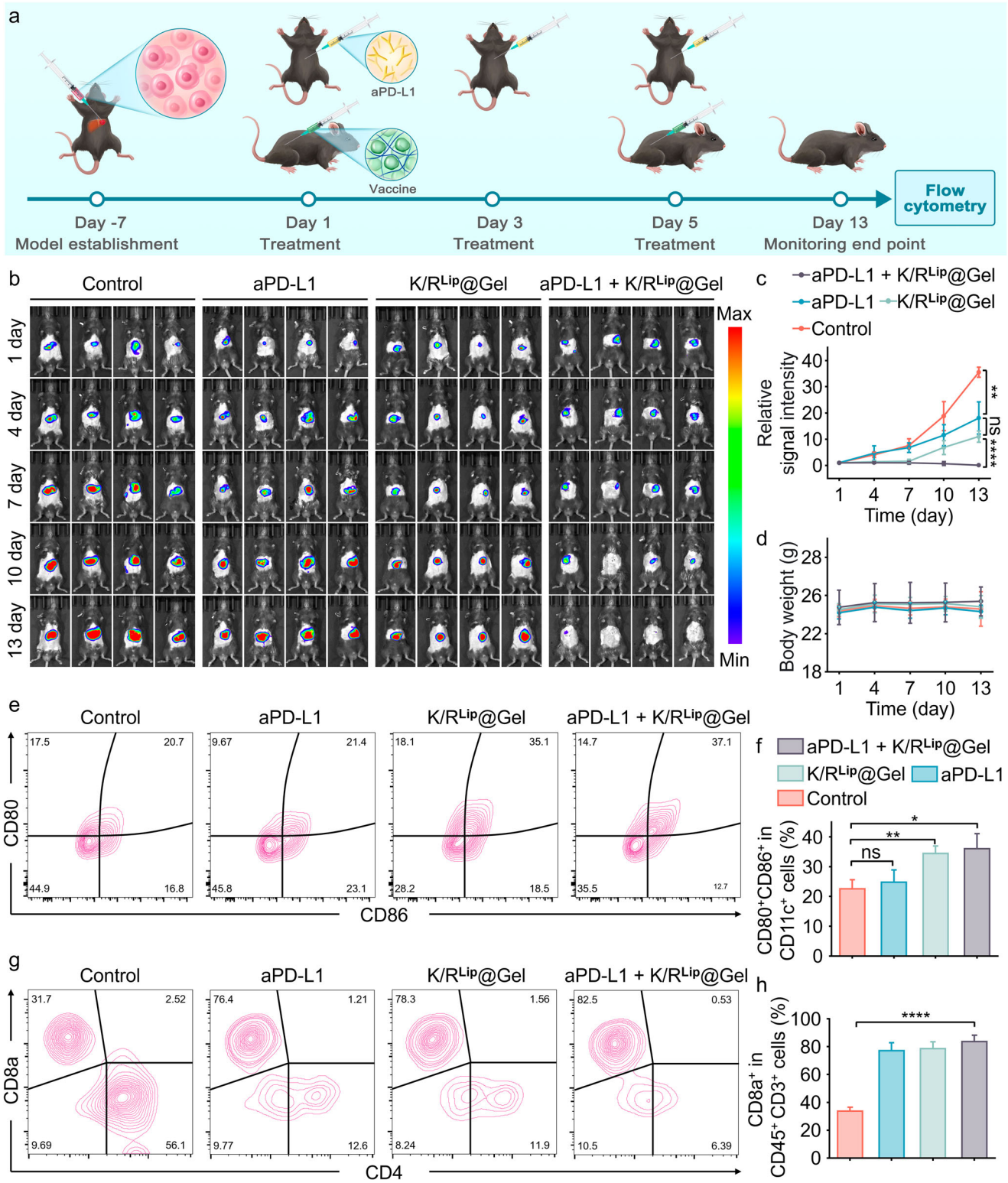

Fig. 4 | K/R^{Lip}@Gel enhanced PD-L1 blockade on orthotopic HCC mice. a Scheme illustration of in vivo treatment and monitoring (Created by the authors with Photoshop v22.5.6). **b** Bioluminescence images of tumor-bearing mice in different groups. **c** Relative signal intensity of tumors in different groups. **d** Body weight of the mice in different groups. **e** Flow cytometry analyzing CD80 and CD86 in CD11c$^+$ dendritic cells in mouse inguinal lymph nodes (Gating strategy was shown in the Supplementary Fig. 14). **f** Quantification of the percentage of CD80$^+$CD86$^+$ cells in CD11c$^+$ dendritic cells. **g** Flow cytometry analyzing CD8a and CD4 of T cells (CD45$^+$CD3$^+$) in tumor tissues (Gating strategy was shown in the Supplementary Fig. 15). **h** Quantification of the percentage of CD8a$^+$ cells in T cells.

After the monitoring period, tumor tissues were obtained to analyze the function of DCs and CD8a$^+$ T cells. Conventional DCs (cDCs), responsible for antigen uptake and presentation, were analyzed with flow cytometry and gated as CD45$^+$lin-1$^{low/-}$HLA-DR$^+$ population, in which the upregulation of CD11c suggested cellular activation. The K/R^{Lip}@Gel and aPD-L1 + K/R^{Lip}@Gel groups exhibited the highest CD11c$^+$ cDCs, suggesting significant activation of antigen presentation stimulated by the vaccine (Fig. 5d, e). Furthermore, granzyme B (GrB) and interferon-γ

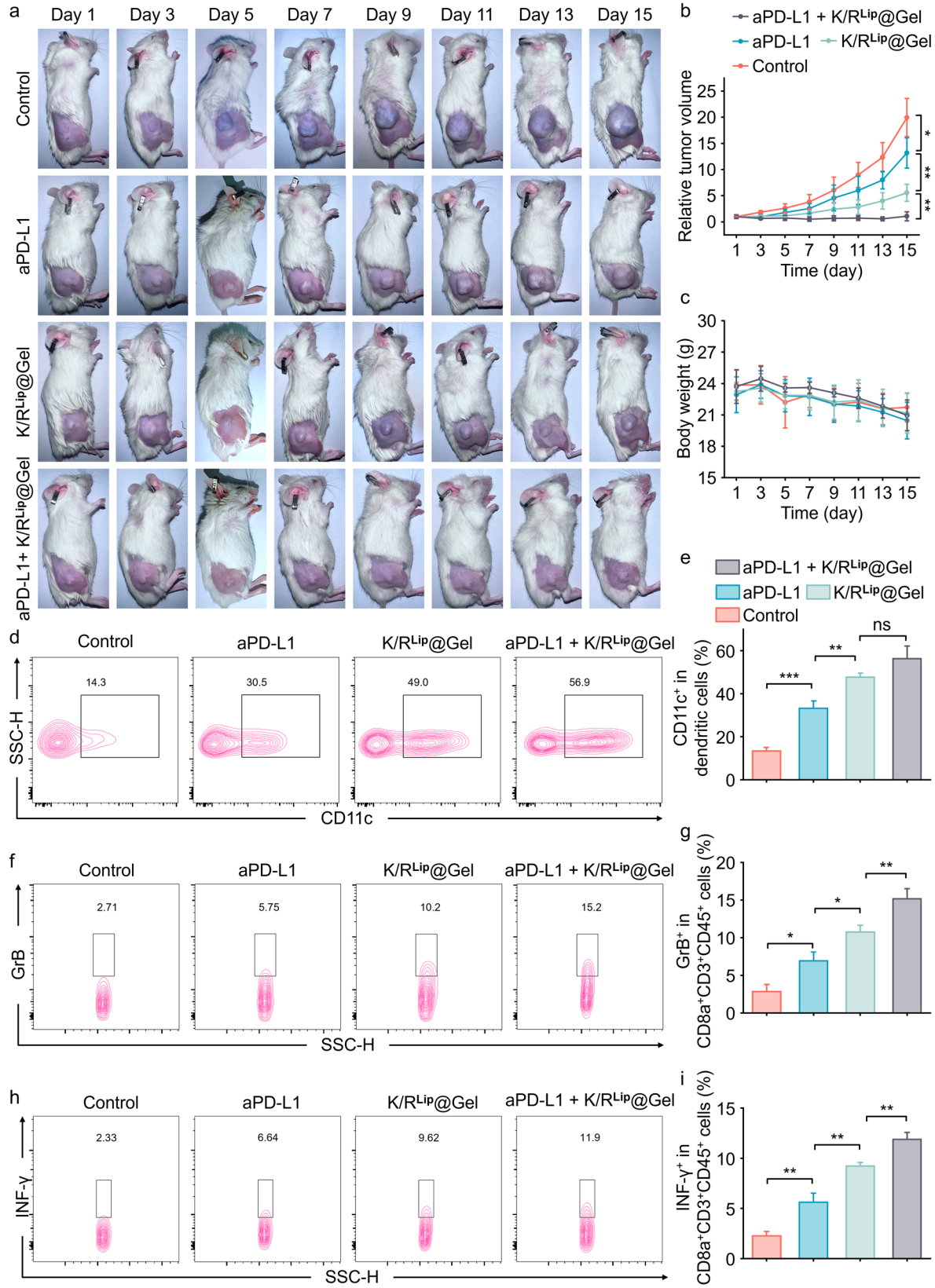

Fig. 5 | K/R^{Lip}@Gel enhanced PD-L1 blockade on orthotopic HCC mice. **a** Photographs of representative mouse in each group during the treatment. **b** Quantification of tumor volume in the 4 groups. **c** Quantification of body weight of the 4 groups. **d** Flow cytometry analyzing CD11c level in dendritic cells (Gating strategy was shown in the Supplementary Fig. 26). **e** Quantification of the percentage of CD11c$^+$ cells in dendritic cells. **f** Flow cytometry analyzing GrB level in CD8$^+$ T cells (Gating strategy was shown in the Supplementary Fig. 27). **g** Quantification of GrB$^+$ cell proportion in CD8a$^+$ T cells. **h** Flow cytometry analyzing INF-γ level in CD8a$^+$ T cells (Gating strategy was shown in the Supplementary Fig. 27). **i** Quantification of INF-γ$^+$ cell proportion in CD8a$^+$ T cells.

(INF-γ) levels in the intratumoral $CD8a^+$ T cells were investigated (Fig. 5f, h). Significant GrB and INF-γ upregulation was observed in the aPD-L1 + K/R^{Lip}@Gel group, depicting the most effective anti-tumor response mediated by $CD8a^+$ T cells (Fig. 5g, i). Moreover, the flow cytometry analysis of $CD8a^+$ T cells in peripheral blood demonstrated similar results, indicating the systemic activation of $CD8a^+$ T cells (Supplementary Fig. 28). The H&E staining of tumor revealed an increased proportion of infiltrated cells and reduced tumor cell nuclei density in the aPD-L1 + K/R^{Lip}@Gel group (Supplementary Fig. 29). Meanwhile, TUNEL staining of tumor depicted the most evident apoptosis within the aPD-L1 + K/R^{Lip}@Gel group (Supplementary Fig. 30).

Discussion

Despite the promise of immune checkpoint blockade (ICB) therapy during HCC treatment, its efficacy is significantly limited by insufficient anti-tumor immune activation[38]. Therefore, the strategies that effectively activate host immunity, such as cancer vaccines, are emerging as collaborators to improve the outcomes of ICB therapies.

In this study, we focused on KIF20A, a protein significantly overexpressed in HCC and plays a critical role in disease progression. Previous studies have established the prognostic value of KIF20A in HCC patients and demonstrated that suppressing KIF20A can improve therapeutic efficacy of ICB, depicting its promise as a therapeutic target[21,22]. In addition, KIF20A has been studied as a vaccine for different cancers, while its suitability for HCC remains unknown. Therefore, we explore KIF20A as a potential candidate for HCC vaccine development and synergize with ICB therapy.

For the first time, the study validated the capacity of KIF20A to elicit anti-tumor immune responses in HCC through transcriptomic mRNA sequencing analysis. The GO enrichment analysis, KEGG enrichment analysis, GSEA, and ssGSEA showed significant activation of different immune responses, particularly those regulated by $CD4^+$ and $CD8^+$ T cells. These responses were likely driven by the multiple antigenic epitopes from the KIF20A protein presented by APCs. Recent perspectives identified full-length proteins as potent antigenic candidates while developing cancer vaccine[11,39–41]. This study used recombinant KIF20A protein to evaluate its immunostimulatory effects in HCC preliminarily. The findings confirmed the suitability of the KIF20A vaccine for HCC and its potential for improving PD-L1 blockade outcomes.

In addition to the antigen, the rational design of the vaccine formulation is crucial for optimizing immunogenicity. Therefore, a novel KIF20A vaccine formulation (K/R^{Lip}@Gel) was developed and the TLR7/8 agonist R848 was paired as an adjuvant[42]. Cationic DOTAP-based liposomes were designed to facilitate efficient encapsulation of the negatively charged KIF20A protein at an optimal DOTAP-to-protein ratio of 20:1. DSPE-PEG and cholesterol were incorporated to improve the liposome stability, thereby elevating immune responses by protecting the payload and promoting the targeting efficiency of lymph nodes[43,44]. Further, a thermosensitive hydrogel (K/R^{Lip}@Gel) was incorporated to ensure sustained liposome release[45,46]. The hydrogel formulation was based on PLGA-PEG-PLGA copolymers, which underwent gelation at body temperature post-subcutaneous injection. This facilitated the prolonged antigen and adjuvant release, enabling a robust immune response.

The in vitro study showed remarkable immunoactivation capabilities, evidenced by the enhanced maturation of BMDCs and increased proliferation and tumor-infiltrating capacity of T cells. In vivo experiments indicated that PD-L1 blockade significantly decreased tumor burden when combined with the vaccine in subcutaneous and orthotopic CDX models. Moreover, flow cytometry confirmed the enhanced activation of DCs and T cells locally and systemically. Further validation in immune-humanized PDX models highlighted the vaccine's potential in a human-relevant setting. The elevated proportion of cDCs responsible for antigen presentation and enhanced activation of $CD8^+$ T cells were observed with flow cytometry, suggesting a potent anti-tumor effect.

In summary, our study is the first to confirm KIF20A as a viable antigen for HCC vaccine development. The K/R^{Lip}@Gel vaccine exhibited potent synergy with PD-L1 blockade therapy. This was demonstrated by significant tumor regression and immune activation in CDX and immune-humanized PDX models. These findings highlighted the potential clinical applicability of the K/R^{Lip}@Gel vaccine in improving ICB therapy outcomes for HCC.

This research has several limitations. First, although we investigated full-length KIF20A protein as the antigen to treat HCC in mouse models, specific $CD4^+$ or $CD8^+$ epitope peptides were not screened in this study. Even though the full-length protein with multiple antigen epitopes could elicit robust immune responses, the responses are less controllable than those elicited by peptides[47,48]. Additionally, producing protein antigens involves more complex processes than peptides, leading to challenges in clinical translation. Therefore, HLA-compatible epitope peptides of KIF20A should be screened in future studies for more predictable and precise immune responses in HCC. Although KIF20A peptides have been explored in small-scale clinical trials for other cancers, these epitopes may differ depending on tumor-specific factors, including antigen processing and immune cell recognition. This highlights the need for additional research in HCC-specific context[49,50]. When compared to another effective vaccine modality, mRNA, proteins are more challenging to achieve high EE in liposome formulations. However, protein antigens offer several advantages, including superior stability against degradation during storage and handling, the ability to directly induce robust immune responses, and technically simpler to avoid the antigen fragmentation during encapsulation. Secondly, while immune-humanized PDX models provide a suitable preclinical platform, using human PBMCs introduces the risk of GVHR, potentially shortening the time window of monitoring treatment[51–53]. Utilizing $CD34^+$ hematopoietic stem cells to develop these models may mitigate GVHR and provide a longer-term assessment of therapeutic efficacy[54]. Finally, comprehensive clinical trials are necessary to fully assess the safety and therapeutic potential of the K/R^{Lip}@Gel vaccine or other KIF20A-based vaccines combined with ICB therapy among human patients.

To sum up briefly, this study identified KIF20A as a viable antigen for HCC vaccine development through transcriptomic mRNA sequencing. Based on this, KIF20A was incorporated into a rationally designed thermosensitive hydrogel formulation (K/R^{Lip}@Gel), producing efficient antigen delivery, sustained release, and robust immunostimulatory effects. Moreover, K/R^{Lip}@Gel potentiated the therapeutic effect of PD-L1 blockade therapy. This was evidenced by significant tumor regression and superior immune activation in subcutaneous and orthotopic CDX models. Furthermore, immune-humanized PDX models validated the translational potential of this approach, indicating enhanced intratumoral $CD8^+$ T cell activity and cDC function. These findings validated the capability of KIF20A-based vaccines to elicit robust anti-tumor immune responses, facilitating the development of a novel method to synergize with immune checkpoint inhibitors.

Methods

Animals and cell culture

8-week-old male C57BL/6J mice and NOD.CB17-*Prkdc*^{scid}*Il2rg*^{tm1}/Bcgen (B-NDG) mice were obtained from Biocytogen (China) and housed under specific pathogen-free (SPF) conditions. All animal experiments in this study were conducted in accordance with the guidelines approved by the Ethics Committee for Animal Experimentation of Zhujiang Hospital (No. LAEC-2023-093). All the animals recruited in the study were anesthetized with 2% isoflurane delivered at a flow rate of 1 L/min prior to experimental procedures. For humane euthanasia, carbon dioxide was delivered at a controlled flow rate of 0.3 L/min in a 1-L capacity chamber. Euthanasia was performed both prior to primary cell isolation and at the end of the treatment monitoring period, in accordance with approved ethical standards.

For cell culture, Hepa1-6 cells and luciferase-transfected Hepa1-6 (Hepa1-6-luc) cells were cultured in Dulbecco's Modified Eagle Medium (DMEM), supplemented with 10% fetal bovine serum (FBS; Procell, China) and 1% Penicillin–Streptomycin (Gibco, USA). L929 cells were cultured in

Minimum Essential Medium (MEM) with the same supplements. All cells were maintained at 37 °C in a humidified incubator with 5% CO_2. Cell lines were regularly tested for mycoplasma contamination.

Transcriptomic mRNA sequencing analysis

Hepa1-6 tumor bearing mice were randomly divided into 2 groups ($n = 4$). Mice in the KIF20A group received a subcutaneous injection of 5 μg KIF20A protein in sterile phosphate buffered solution (PBS), while the control group was injected with an equal volume of sterile PBS. After 3 days, the mice were sacrificed, and the tumor were harvested for transcriptomic mRNA sequencing.

Total RNA was extracted using Trizol reagent (Invitrogen, USA), and RNA quality was assessed using an Agilent 2100 Bioanalyzer (Agilent Technologies, USA) as well as RNase-free agarose gel electrophoresis. Eukaryotic mRNA was enriched from the total RNA using Oligo (dT) beads (Epicentre, USA). The enriched mRNA was fragmented using a fragmentation buffer and reverse transcribed into cDNA with the NEBNext Ultra RNA Library Prep Kit for Illumina (NEB #7530, USA). Double-stranded cDNA was purified, followed by end repair, A-tailing, and ligation to Illumina sequencing adapters. The ligation products were purified with AMPure XP Beads (1.0×) and amplified by PCR to generate the cDNA library, which was sequenced using the NovaSeq6000 system (Illumina, USA).

Differential gene expression analysis was performed using R (version 4.10) with the ClusterProfiler package[51]. The genes/transcripts with false discovery rate (FDR) below 0.05 and absolute fold change ($\log_2$FC) ≥ mean ± 2 × SD were classified as DEGs. GO, KEGG enrichment analysis, and Gene Set Enrichment Analysis (GSEA) were conducted to identify functional and pathway enrichments of the DEGs, with gene sets obtained from the Molecular Signatures Database (MSigDB).

Preparation of KIF20A and R848 co-encapsulating liposome (K/R^{Lip})

KIF20A and R848 co-encapsulating liposomes (K/R^{Lip}) were prepared using a thin film hydration method. Briefly, 28 mg (2,3-Dioleoyloxy-propyl)-trimethylammonium-chloride (DOTAP, Aladdin Scientific, China), 1.3 mg cholesterol (Aladdin Scientific, China)and 11.2 mg DSPE-PEG2000 (Aladdin Scientific, China) were dissolved in 40.5 mL chloroform to create a stock solution. Then, 2 mg R848 (Aladdin Scientific, China) was added into 10 mL stock solution. The mixture was subjected to rotary evaporation at 40°C until the solvent was completely removed to form a thin film. The evaporation step was repeated after the addition of another 10 mL chloroform. After the final evaporation, 0.5 mg KIF20A protein (Abmart, China) dissolved in 2 mL ultrapure water was used for hydration. The resulting suspension was then extruded through a mini extruder (Avanti, USA) equipped with 200 nm and 100 nm polycarbonate membranes (Millipore, USA), successively, for 11 passes each membrane to generate unilamellar liposomes. The liposomes were then dialyzed in a 200 kDa molecular weight cutoff (MWCO) dialysis tube for 12 h to remove any unencapsulated components, followed by lyophilization for another 12 h. The resulting K/R^{Lip} powder was stored at -20°C for further use. For the preparation of indocyanine green (ICG)-labeled Vac (ICG-K/R^{Lip}), 0.2 mg ICG was added in the hydration step.

Control formulations were also prepared, including R848-only liposomes (R^{Lip}) and KIF20A-only liposomes (K^{Lip}), using the same thin-film hydration method as described above.

Characterization of K/R^{Lip} and ICG-K/R^{Lip}

The morphology of K/R^{Lip} and ICG-K/R^{Lip} was observed using a TEM (FEI, USA). DLS and Zeta potential were measured with a Zetasizer (Malvern Panalytical, UK). The absorbance and fluorescence spectra were measured using a fluorescence spectrophotometer (Agilent, USA). The encapsulation efficiency and encapsulation capacity were determined with an ultramicro spectrophotometer (Thermo Scientific, USA) and calculated according to the following formulas:

$$Encapsulation\ \text{efficiency} = \frac{Weight\ of\ druge\ ncapsulated}{Total\ weight\ of\ drugadded} \times 100\%$$

$$Encapsulation\ capacity = \frac{\text{W}eight\ \text{of drug encapsulated}}{Total\ weight\ of\ the\ delivery\ system} \times 100\%$$

Synthesis of PLGA-PEG-PLGA triblock copolymers

To synthesize PLGA-PEG-PLGA triblock copolymers, 60 g PEG1500 was heated to 120 °C for 30 min in the nitrogen atmosphere with magnetic stirring, followed by an additional 2 h under nitrogen flow to completely remove any moisture. Afterwards, 113.46 g DL-lactide and 30.48 g glycolide (molar ratio 3:1) were added to the PEG1500 and heated at 120°C under nitrogen flow. After 30 min, 0.04 g of stannous octoate was added and the reaction mixture was maintained at 150 °C for 8 h. Upon completion of the reaction, the system was cooled to room temperature. Then, 40 mL dichloromethane was added to dissolve the crude product, followed by precipitation with 500 mL petroleum ether to precipitate the product. The precipitate was collected by filtration. This dissolution-precipitation process was repeated three times to ensure a high-purity product. The successful synthesis of PLGA-PEG-PLGA triblock copolymers was confirmed using ^{1}H-NMR (Bruker, Germany).

Preparation of thermosensitive hydrogel vaccine (K/R^{Lip}@Gel) and its characterization

PLGA-PEG-PLGA triblock copolymer were dissolved in ultrapure water to a final concentration of 15% (w/v). To generate K/R^{Lip}@Gel, 1 mg of K/R^{Lip} was added to 1 mL of the PLGA-PEG-PLGA solution and stirred at 4 °C for 1 h. Similarly, single-drug encapsulating liposomes containing either R848 or KIF20A protein were incorporated into the PLGA-PEG-PLGA solution to create R^{Lip}@Gel and K^{Lip}@Gel, respectively. The gelation properties of K/R^{Lip}@Gel were characterized using a rheometer (Anton Paar, Austria) at different temperature or under constant shear stress of 1% amplitude with 1 rad/s for 6 min.

Evaluation of in vivo sustained release

C57BL/6J mice were divided into three groups and subcutaneously injected 100 μL with small-molecule ICG, nanoscale K/R^{Lip} or hydrogel K/R^{Lip}@Gel. NIR-II fluorescence images were captured at 6, 12, 24, 48, 72 and 96 h post-injection using an 808-nm excitation laser and an 1100 nm long-pass filter to assess the sustained release properties of each formulation.

Isolation of BMDCs and spleen cells

BMDCs were isolated from 8-week-old C57BL/6J mice. Cells from the femur and tibia were flushed out with PBS and filtered through a 70 μm strainer (Corning, USA). The filtered suspension was centrifuged at 800×g for 5 min, and the supernatant was discarded. Red blood cells (RBCs) were lysed using ACK buffer (Elabscience, China), followed by a second centrifugation at 800×g for 5 min. The remaining cells were resuspended in Roswell Park Memorial Institute 1640 (RPMI1640) medium (Gibco, USA) supplemented with 10% FBS, 1% penicillin-streptomycin (Gibco, USA), 50 μM β-mercaptoethanol (Procell, China), 20 ng/mL murine granulocyte-macrophage colony-stimulating factor (GM-CSF, Peprotech, USA), and 10 ng/mL interleukin-4 (IL-4, MedChemExpress, USA). Cells were seeded into 6-well plates, and the cytokine-containing medium was replaced on days 3 and 5. After a 7-day incubation, the BMDCs were harvested for further experiments.

For the isolation of spleen cells, spleens from 8-week-old C57BL/6J mice were harvested, mechanically filtered against a 70 μm sterile strainer, and rinsed with PBS. The cell suspension was centrifuged at 800 × g for 5 minutes, and the supernatant was discarded. RBCs were lysed, and the remaining cells were resuspended in RPMI1640 medium supplemented

with 10% FBS and 1% penicillin-streptomycin. The spleen cells were then cultured for further experiments.

Cytotoxicity and hemolysis test

L929 fibroblast cells were seeded into 96-well plates at a density of 1×10^4 cells per well and incubated with either Gel or K/R^{Lip}@Gel for 1, 3 and 5 days. The cytotoxicity of the formulations was assessed using the Cell Counting Kit-8 (CCK-8) assay according to the manufacturer's instructions. Absorbance was measured at 450 nm using a microplate reader, and cell viability was calculated to evaluate the potential cytotoxic effects of Gel and K/R^{Lip}@Gel over time.

Blood was collected from a C57BL/6J mouse into a heparinized anticoagulant tube and washed three times with PBS to isolate RBCs. The RBCs were then incubated with varying concentrations of Gel or K/R^{Lip}@Gel for 4 hours at 37 °C. After incubation, the suspensions were centrifuged at 800×g for 5 min, and the supernatant was collected. Absorbance was measured at 532 nm to assess hemoglobin release, and the hemolysis rate was calculated using PBS as a negative control and distilled water as a positive control.

Flow Cytometry of BMDCs

BMDCs were divided into different groups and incubated with 100 μL solidified K^{Lip}@Gel, R^{Lip}@Gel or K/R^{Lip}@Gel in 6-well plates for 24 h. Then the BMDCs were collected, and the Fc receptors (FcR) were blocked using anti-mouse CD16/32 antibody (Biolegend, USA). Cells were subsequently stained with APC-conjugated anti-mouse CD11c, FITC-conjugated anti-mouse CD80, and PE-conjugated anti-mouse CD86 antibodies (Elabscience, China) for flow cytometry analysis (Beckman, USA). The CD80$^+$CD86$^+$ cells within the CD11c$^+$ dendritic cell population were gated and quantified to assess BMDC maturation and activation.

T cell proliferation rate

BMDCs were pulsed with K^{Lip}@Gel, R^{Lip}@Gel or K/R^{Lip}@Gel for 24 h. Afterwards, Spleen cells labeled with CFDA-SE (MedChemExpress, USA) were co-cultured with the pulsed BMDCs for 3 days. After co-culture, the cells were harvested, and FcR was blocked using anti-mouse CD16/32 antibody. The cells were then stained with APC-conjugated anti-mouse CD3 antibody (Elabscience, China), and the CFDA-SE fluorescence intensity of CD3$^+$ cells was analyzed by flow cytometry to assess T cell proliferation rate.

T cell infiltration

BMDCs were pulsed with K^{Lip}@Gel, R^{Lip}@Gel or K/R^{Lip}@Gel for 24 h. Subsequently, spleen cells were labeled with CellTracker^{TM} deep red (MKBio, China) and added to the BMDC-containing 6-well plates. After 3 days of co-culture, the cells were collected, and CD8$^+$ T cells were isolated using the miniMACS^{TM} system and CD8a$^+$ T cell isolation kit (Miltenyi Biotec, Germany). The isolated CD8a$^+$ T cells were counted and diluted to a concentration of 1×10^5 cells/mL. Then, the cell suspension was added into a round-bottom ultra-low attachment 96-well plate (Corning, USA) that contains Hepa1-6 cell spheroids to incubate for 24 h. Afterwards, the spheroids were fixed with 4% paraformaldehyde for 15 min and stained with DAPI for 10 min. CLSM (Nikon, Japan) was used to observe the CD8a$^+$ T cells infiltrated into the Hepa1-6 spheroids.

Establishment of Hepa1-6 tumor models

To establish the subcutaneous CDX models, 1×10^6 Hepa1-6 cells suspended in 100 μL PBS were subcutaneously injected into the right hind limb or axillary region of 8-week-old male C57BL/6J mice. Mice with tumors that exhibited rapid growth without signs of necrosis or scab formation were selected for subsequent experimental studies.

For the establishment of orthotopic CDX models, male C57BL/6J mice (8 weeks old) were anesthetized using isoflurane, and an incision (roughly 8 mm) for each mouse was made along the abdominal midline. Subsequently, 1×10^6 Hepa1-6-luc cells suspended in a mixture of 10 μL PBS and 10 uL Matrigel (BD Biosciences, USA) were injected into the left lobe of the liver. The incision was then sutured using 6-0 threads. The successful establishment of orthotropic CDX models was comfirmed using bioluminescence imaging following intraperitoneal administration of D-luciferin potassium salt (150 mg/kg, GlpBio, USA).

In vivo tumor prevention effect of K/R^{Lip}@Gel

C57BL/6J mice were subcutaneously vaccinated with K/R^{Lip}@Gel (1 mg/mL, 100 μL) or sterile PBS and divided into 2 groups. 3 days post-vaccination, Hepa1-6-luc cells were injected orthotopically ($n=3$) or subcutaneously ($n=3$). Tumor growth rate was subsequently monitored with an IVIS Imaging Spectrum System (PerkinElmer, USA) using bioluminescence mode.

In vivo K/R^{Lip}@Gel and PD-L1 blockade therapy on Hepa1-6 tumor model

Hepa1-6 subcutaneous tumor-bearing mice were randomly divided into 4 groups ($n=5$). Each group received different treatments: subcutaneous vaccination with K/R^{Lip}@Gel (5 mg/kg), intraperitoneal injection of anti-mouse PD-L1 antibody (10 mg/kg) (Bio X Cell, USA, Clone: 10F.9G2™)or a combination of both. Body weight and tumor volume were recorded every 3 days after drug administration. The tumor volume was calculated using the formula: tumor volume = length × width^2/2. At the end of the treatment period, all mice were humanely euthanized. Organs and tumor tissues were harvested for histological analysis and the blood samples were collected for biochemical index testing.

Hepa1-6 orthotopic tumor-bearing mice were randomly assigned to the same 4 treatment groups as in the subcutaneous tumor model ($n=4$). Body weight was recorded after injection. Additionally, the bioluminescent signal from orthotopic tumors was measured using bioluminescence imaging. At the end of the monitoring period, mice were humanely euthanized, and tumor tissues, inguinal lymph nodes, spleen, and blood samples were collected for flow cytometry analysis.

Establishment of immune-humanized PDX model

To establish the immune-humanized PDX model, primary tumor samples were obtained from a patient undergoing HCC resection surgery at Zhujiang Hospital and engrafted into B-NDG mice for 3 passages. The protocol involving human HCC samples was approved by the Medical Ethics Committee of Zhujiang Hospital (No. 2024-KY-219). PBMCs were isolated from the peripheral blood of a healthy volunteer with PBMC isolation tubes (Stemcell Technology, USA) and Histopaque®-1077 (Sigma-Aldrich, USA) and intravenously injected into the B-NDG mice (5×10^8 cells per mouse). Then, tumor tissues were planted into the PBMC injection mice as the 4th passages. The percentage of hCD45$^+$ cells in the mouse peripheral blood was monitored weekly using flow cytometry. After 4 weeks, the successful establishment of the immune-humanized PDX model was confirmed when the tumor volume reached approximately 100 mm^3 and the proportion of hCD45$^+$ cell in mouse peripheral blood exceeded 25%.

In vivo K/R^{Lip}@Gel and PD-L1 blockade therapy on PDX model

Immune-humanized PDX models were divided into 4 groups ($n=3$) and received treatments with K/R^{Lip}@Gel (5 mg/kg), anti-human PD-L1 antibody (10 mg/kg) (Bio X Cell, USA, Clone: Atezolizumab), or a combination of both. For the PDX models, the antigen used in K/R^{Lip}@Gel was human KIF20A protein instead of the mouse protein. Body weight and tumor size were monitored regularly after drug administration. At the end of the monitoring period, blood samples and tumor tissues were collected for flow cytometry and histological analysis to evaluate the therapeutic effects.

Flow cytometry analysis of tissue and blood

Single-cell suspensions were prepared from tissues prior to flow cytometry analysis. Tumor tissue fragments (1–2 mm^3) were digested with collagenase I (200 U/mL), hyaluronidase (100 U/mL), and DNase I (50 U/mL) at 37 °C for 45 min with shaking at 90 rpm. Spleen tissues were lysed using collagenase IV (150 U/mL) and DNase I (50 U/mL) under the same conditions.

Inguinal lymph nodes were digested with collagenase I (200 U/mL), hyaluronidase (100 U/mL), and DNase I (50 U/mL). Blood samples were washed with PBS at 800 rpm for 5 minutes with 3-time repeat. All samples underwent red blood cell (RBC) lysis before antibody labeling.

For the Hepa1-6 tumor model (CDX model), cells were first blocked with anti-mouse CD16/32 antibody. Intratumoral, splenic, and peripheral blood T cells were labeled with PerCP-conjugated anti-mouse CD45, APC-conjugated anti-mouse CD3, PE-conjugated anti-mouse CD4, and FITC-conjugated anti-mouse CD8a antibodies. Lymphatic dendritic cells were labeled with APC-conjugated anti-mouse CD11c, FITC-conjugated anti-mouse CD80, and PE-conjugated anti-mouse CD86 antibodies. All antibodies used for the CDX model were purchased from Elabscience (China).

For the PDX model, cells were blocked with FcR Blocking Solution (Biolegend, USA). cDCs were labeled with PerCP-conjugated anti-human CD45, FITC-conjugated anti-human Lineage Cocktail-1 (Lin-1, containing anti-CD3, CD14, CD16, CD19, CD20, and CD56 antibodies) (Biolegend, USA), APC-conjugated anti-human HLA-DR (Elabscience, China), and PE-conjugated anti-human CD11c (Elabscience, China). T cells were labeled with PerCP-conjugated anti-human CD45 (Elabscience, China), APC-conjugated anti-human CD3 (Elabscience, China), FITC-conjugated anti-human CD8a (Elabscience, China), PE/Cyanine7-conjugated anti-human IFN-γ (Biolegend, USA), and PE-conjugated anti-human Granzyme B (AntibodySystem, USA). The FIX & PERM™ Cell Permeabilization Kit (Invitrogen, USA) was used before labeling with PE/Cyanine7 anti-human IFN-γ and PE anti-human Granzyme B.

statistical analysis

All statistical analyzes were performed using GraphPad Prism 10.0 (GraphPad Software, USA). Differences among 2 groups were analyzed using the student's T test unless otherwise indicated. Values of $P < 0.05$ were considered statistically significant. The significant differences were noted in the figures: ns (no significant difference), *($P < 0.05$), **($P < 0.01$), ***($P < 0.001$), ****($P < 0.0001$).

Data Availability

The datasets used or analyzed during the current study are available from the corresponding author on reasonable request.

Received: 19 September 2024; Accepted: 28 December 2024;
Published online: 03 January 2025

References

1. Bray, F. et al. Global cancer statistics 2022: GLOBOCAN estimates of incidence and mortality worldwide for 36 cancers in 185 countries. *CA Cancer J. Clin.* **74**, 229–263 (2024).
2. Finn, R. S. et al. Atezolizumab plus bevacizumab in unresectable hepatocellular carcinoma. *New Engl. J. Med.* **382**, 1894–1905 (2020).
3. Foerster, F., Gairing, S. J., Ilyas, S. I. & Galle, P. R. Emerging immunotherapy for HCC: a guide for hepatologists. *Hepatology* **75**, 1604–1626 (2022).
4. Yang, J. D. et al. A global view of hepatocellular carcinoma: trends, risk, prevention and management. *Nat. Rev. Gastro. Hepat.* **16**, 589–604 (2019).
5. Brown, Z. et al. Management of hepatocellular carcinoma: a review. *JAMA Surg.* **158**, 410–420 (2023).
6. Yau, T. et al. Nivolumab versus sorafenib in advanced hepatocellular carcinoma (CheckMate 459): a randomised, multicentre, open-label, phase 3 trial. *The lancet oncology* **23**, 77–90 (2022).
7. Luo, X., Wu, K. & He, X. Advances in drug development for hepatocellular carcinoma: clinical trials and potential therapeutic targets. *J. Exp. Clin. Cancer Res.* **40**, 172 (2021).
8. Pinter, M., Jain, R. K. & Duda, D. G. The Current landscape of immune checkpoint blockade in hepatocellular carcinoma: A Review. *JAMA Oncol.* **7**, 113–123 (2021).
9. Liu, Y. et al. Identification of a tumour immune barrier in the HCC microenvironment that determines the efficacy of immunotherapy. *J. Hepatol.* **78**, 770–782 (2023).
10. Yang, C. et al. Evolving therapeutic landscape of advanced hepatocellular carcinoma. *Nat. Rev. Gastro. Hepat.* **20**, 203–222 (2023).
11. Lin, M. J. et al. Cancer vaccines: the next immunotherapy frontier. *Nat. Cancer* **3**, 911–926 (2022).
12. Brandenburg, A., Heine, A. & Brossart, P. Next-generation cancer vaccines and emerging immunotherapy combinations. *Trends Cancer* **10**, 749–769 (2024).
13. Saxena, M., van der Burg, S. H., Melief, C. J. M. & Bhardwaj, N. Therapeutic cancer vaccines. *Nat. Rev. Cancer* **21**, 360–378 (2021).
14. Lu, L. et al. Targeting neoantigens in hepatocellular carcinoma for immunotherapy: a futile strategy? *Hepatology* **73**, 414–421 (2021).
15. Lu, L. et al. Targeting tumor-associated antigens in hepatocellular carcinoma for immunotherapy: past iitfalls and future strategies. *Hepatology* **73**, 821–832 (2021).
16. Hu, Z., Ott, P. A. & Wu, C. J. Towards personalized, tumour-specific, therapeutic vaccines for cancer. *Nat. Rev. Immunol.* **18**, 168–182 (2018).
17. Sellars, M., Wu, C. & Fritsch, E. Cancer vaccines: building a bridge over troubled waters. *Cell* **185**, 2770–2788 (2022).
18. Leko, V. & Rosenberg, S. A. Identifying and targeting human tumor antigens for T Cell-based immunotherapy of solid tumors. *Cancer Cell* **38**, 454–472 (2020).
19. Xie, B. et al. Proteomic mapping and targeting of mitotic pericentriolar material in tumors bearing centrosome amplification. *Cancer Res.* **82**, 2576–2592 (2022).
20. Wei, J. et al. Cucurbitacin B-induced G2/M cell cycle arrest of conjunctival melanoma cells mediated by GRP78–FOXM1–KIF20A pathway. *Acta Pharm. Sin. B* **12**, 3861–3876 (2022).
21. Collette, Y. et al. Abstract 1813: DIACC2010, a selective inhibitor of KIF20A. *Cancer Res.* **82**, 1813–1813 (2022).
22. Chen, S. et al. Inhibition of KIF20A enhances the immunotherapeutic effect of hepatocellular carcinoma by enhancing c-Myc ubiquitination. *Cancer Lett.* **598**, 217105 (2024).
23. Akazawa, Y. et al. Abstract A001: phase I study of vaccine therapy with a cocktail of peptides for pediatric patients with refractory solid tumors. *Cancer Immunol. Res.* **7**, A001 (2019).
24. Bandi, D., Sarvesh, S., Farran, B., Nagaraju, G. & El-Rayes, B. Targeting the metabolism and immune system in pancreatic ductal adenocarcinoma: Insights and future directions. *Cytokine Growth F. R.* **71**, 26–39 (2023).
25. Bayo, J. et al. A comprehensive study of epigenetic alterations in hepatocellular carcinoma identifies potential therapeutic targets. *J. Hepatol.* **71**, 78–90 (2019).
26. Hu, Y. et al. Identification of chromosomal instability-associated genes as hepatocellular carcinoma progression-related biomarkers to guide clinical diagnosis, prognosis and therapy. *Comput. Biol. Med.* **148**, 105896 (2022).
27. Yang, Z. et al. Reinforced immunogenic endoplasmic reticulum stress and oxidative stress via an orchestrated nanophotoinducer to boost cancer photoimmunotherapy. *ACS Nano* **18**, 7267–7286 (2024).
28. Dang, X. T. T. et al. Dendritic cell-targeted delivery of antigens using extracellular vesicles for anti-cancer immunotherapy. *Cell Prolif.* **57**, e13622 (2024).
29. Wang, J. et al. Endoplasmic reticulum-targeted delivery of celastrol and PD-L1 siRNA for reinforcing immunogenic cell death and potentiating cancer immunotherapy. *Acta Pharm. Sin. B* **14**, 3643–3660 (2024).
30. Raynor, J. L. & Chi, H. Nutrients: Signal 4 in T cell immunity. *J. Exp. Med*. **221** (2024).
31. Kok, V. C., Wang, C. C. N., Liao, S.-H. & Chen, D.-L. Abstract 2719: Interleukin-17 and cytokine-related signalings are determinants for

tumor immune microenvironment in triple-negative breast cancer: in silico integrated analysis. *Cancer Res.* **81**, 2719–2719 (2021).
32. Shi, R.-Y. et al. Trafficking circuit of CD8+ T cells between the intestine and bone marrow governs antitumour immunity. *Nat. Cell Biol.* **26**, 1346–1358 (2024).
33. Liang, Z. et al. The orientation of CpG conjugation on aluminum oxyhydroxide nanoparticles determines the immunostimulatory effects of combination adjuvants. *Biomaterials* **308**, 122569 (2024).
34. Li, K. et al. A dual enhancing strategy of novel nanovaccine based on TIM3 silencing nanoadjuvants and desialylated cancer cell membrane antigens for personalized vaccination immunotherapy of cancer. *Adv. Funct. Mater*. 2404956 (2024).
35. Schunke, J. et al. Co-delivery of STING and TLR7/8 agonists in antigen-based nanocapsules to dendritic cells enhances CD8+ T cell-mediated melanoma remission. *Nano Today* **57**, 102365 (2024).
36. Liu, X. et al. Mobilizing STING Pathway via a Cationic Liposome to Enhance Doxorubicin-Induced Antitumor Immunity. *Adv. Funct. Mater*. 2416406 (2024).
37. Li, M. et al. Cationic liposomes co-deliver chemotherapeutics and siRNA for the treatment of breast cancer. *Eur. J. Med. Chem.* **233**, 114198 (2022).
38. Shen, K. Y., Zhu, Y., Xie, S. Z. & Qin, L. X. Immunosuppressive tumor microenvironment and immunotherapy of hepatocellular carcinoma: current status and prospectives. *J. Hematol. Oncol.* **17**, 25 (2024).
39. Yi, Y. et al. Vaccine-like nanomedicine for cancer immunotherapy. *J. Control. Release* **355**, 760–778 (2023).
40. Hernandez-Franco, J. F., Jan, I. M., Elzey, B. D. & HogenEsch, H. Intradermal vaccination with a phytoglycogen nanoparticle and STING agonist induces cytotoxic T lymphocyte-mediated antitumor immunity. *npj Vaccines* **9**, 149 (2024).
41. Jenika, D. et al. In vivo assembly of epitope-coated biopolymer particles that induce anti-tumor responses. *npj Vaccines* **9**, 18 (2024).
42. Chao, P. H., Chan, V., Wu, J., Andrew, L. J. & Li, S. D. Resiquimod-loaded cationic liposomes cure mice with peritoneal carcinomatosis and induce specific anti-tumor immunity. *J. Control. Release* **372**, 362–371 (2024).
43. Smith, R. et al. Cationic nanoparticles enhance T cell tumor infiltration and antitumor immune responses to a melanoma vaccine. *Sci. Adv.* **8**, eabk3150 (2022).
44. Tang, Y. et al. Interactions between nanoparticles and lymphatic systems: mechanisms and applications in drug delivery. *Adv. Drug Deliv. Rev.* **209**, 115304 (2024).
45. Gong, N. et al. Enhancing in situ cancer vaccines using delivery technologies. *Nat. Rev. Drug Discov.* **23**, 607–625 (2024).
46. Liu, J. et al. Intravesical chemotherapy synergize with an immune adjuvant by a thermo-sensitive hydrogel system for bladder cancer. *Bioact. Mater.* **31**, 315–332 (2024).
47. Guo, N. et al. Immunoinformatics design and in vivo immunogenicity evaluation of a conserved CTL multi-epitope vaccine targeting HPV16 E5, E6, and E7 proteins. *Vaccines* **12** (2024).
48. Zhang, R., Billingsley, M. M. & Mitchell, M. J. Biomaterials for vaccine-based cancer immunotherapy. *J. Control. Release* **292**, 256–276 (2018).
49. Yang, C. et al. Identification of tumor rejection antigens and the immunologic landscape of medulloblastoma. *Genome. Med.* **16**, 102 (2024).
50. Perez, M. A. S. et al. Predicting antigen-specificities of orphan T cell receptors from cancer patients with TCRpcDist. *Adv. Sci*., 2405949 (2024).
51. Meng, J. et al. Generation of whole tumor cell vaccine for on-demand manipulation of immune responses against cancer under near-infrared laser irradiation. *Nat. Commun.* **14**, 4505 (2023).
52. Chuprin, J. et al. Humanized mouse models for immuno-oncology research. *Nat. Rev. Clin. Oncol.* **20**, 192–206 (2023).
53. Cassidy, J. W., Caldas, C. & Bruna, A. Maintaining tumor heterogeneity in patient-derived tumor xenografts. *Cancer Res.* **75**, 2963–2968 (2015).
54. Wu, T. et al. clusterProfiler 4.0: a universal enrichment tool for interpreting omics data. *Innovation* **2**, 100141 (2021).

Acknowledgements

This work was supported by the National Natural Science Foundation of China (81627805 and 12026602).

Author contributions

X. Z. and F. X. contribute equally to this project. X. Z. designed the research study, performed the experiments, analyzed the data and wrote the manuscript. F. X. performed the experiments, assisted the data analysis, and revised the manuscript. Z. L. and X. Y. helped performe the experiments, X. Z. helped obtain the patients' HCC tissues. J. C. helped revise the manuscripts and create schematic illustrations. C. F. supervised the study. All authors approved the final version.

Competing interests

The authors declare no competing interests.

Additional information

Supplementary information The online version contains supplementary material available at https://doi.org/10.1038/s41541-024-01060-2.

Correspondence and requests for materials should be addressed to Chihua Fang.